# Ionic solids from common colloids

https://doi.org/10.1038/s41586-020-2205-0

Theodore Hueckel<sup>1</sup>, Glen M. Hocky<sup>1</sup>, Jeremie Palacci<sup>2</sup> & Stefano Sacanna<sup>1⊠</sup>

Received: 14 August 2019

Accepted: 26 February 2020

Published online: 22 April 2020

Check for updates

From rock salt to nanoparticle superlattices, complex structure can emerge from simple building blocks that attract each other through Coulombic forces<sup>1-4</sup>. On the micrometre scale, however, colloids in water defy the intuitively simple idea of forming crystals from oppositely charged partners, instead forming non-equilibrium structures such as clusters and gels<sup>5-7</sup>. Although various systems have been engineered to grow binary crystals<sup>8-11</sup>, native surface charge in aqueous conditions has not been used to assemble crystalline materials. Here we form ionic colloidal crystals in water through an approach that we refer to as polymer-attenuated Coulombic self-assembly. The key to crystallization is the use of a neutral polymer to keep particles separated by well defined distances, allowing us to tune the attractive overlap of electrical double layers, directing particles to disperse, crystallize or become permanently fixed on demand. The nucleation and growth of macroscopic single crystals is demonstrated by using the Debye screening length to fine-tune assembly. Using a variety of colloidal particles and commercial polymers, ionic colloidal crystals isostructural to caesium chloride, sodium chloride, aluminium diboride and K<sub>4</sub>C<sub>60</sub> are selected according to particle size ratios. Once fixed by simply diluting out solution salts, crystals are pulled out of the water for further manipulation, demonstrating an accurate translation from solution-phase assembly to dried solid structures. In contrast to other assembly approaches, in which particles must be carefully engineered to encode binding information<sup>12-18</sup>, polymer-attenuated Coulombic self-assembly enables conventional colloids to be used as model colloidal ions, primed for crystallization.

To assemble ionic colloidal crystals in water, we employ a twist to Derjaguin-Landau-Verwey-Overbeek (DLVO) theory<sup>19</sup> that balances the electrostatic attractive force between oppositely charged particles with steric repulsion from well-defined polymer brushes between them. Attraction is provided by overlapping electrical double layers, that is, clouds of oppositely charged ions surrounding charged particles. The thickness of the double layer is characterized by the Debye screening length  $\lambda_D$ , which sets the range of attraction. The polymer brush serves as a particle spacer and its purpose is twofold: first to prevent particles from entering the van der Waals region, and second to set the overlap of the electrical double layers. Particle separation regulates the amplitude of the electrostatic attraction, effectively forming an ionic bond whose strength can be tuned through  $\lambda_{\rm D}$ . This idea is illustrated in Fig. 1a, where we consider the contribution of the electrostatic potential  $V_{\rm F}$ (dotted) between overlapping oppositely charged double layers and the repulsive potential  $V_P$  (dashed) between polymer brushes. As we typically consider particle spacers of thickness larger than 6 nm, particles do not come in close contact and we can neglect van der Waals interactions.  $V_E$  is obtained as for DLVO theory, but considering particles of opposite surface potentials  $\Psi_{\scriptscriptstyle +}$  and  $\Psi_{\scriptscriptstyle -}$ . This gives:  $\frac{V_E}{k_BT} = 2\pi \varepsilon r \psi_+ \psi_- \exp(-h/\lambda_D)$ , where r is the radius, h is the surfaceto-surface particle separation,  $k_{\rm B}$  is the Boltzmann constant, T is temperature and  $\varepsilon$  is the solvent permittivity<sup>19</sup>. The repulsion between the polymer brushes,  $V_P$ , is given by the Alexander-de Gennes polymer brush model (Methods), built on scaling arguments and predicting forces similar to more advanced theoretical treatments<sup>20</sup>. Superposition of the two yields the pair potential  $V_{\rm FP}$  between oppositely charged particles (solid lines), which exhibit a local minimum conveniently tuned by varying  $\lambda_D$  relative to the thickness of the polymer spacer L. The depth of the minima corresponds to the bond energy  $E_b$  between oppositely charged particles. For  $\lambda_D \ll L$ , the polymer brush prevents the double layers from overlapping, the electrostatic interaction vanishes and the particles are sterically stabilized. For  $\lambda_D >> L$ , the presence of the polymer brush is negligible, the double layers fully overlap, and the particles aggregate. For  $\lambda_D$  comparable to L, repulsion from the brush and electrostatic attraction nicely balance to establish an ionic bond  $E_b$  of a few  $k_{\rm B}T$ . Here the particle spacers maintain separation between oppositely charged particles while attracting one another electrostatically, providing cohesion with reconfigurablility-an indispensable condition for dependable assembly. Qualitatively, the equilibrium distances prove to be close to the contact point between the two brushes,  $h \approx 2L$ , as for a nearly impenetrable wall, which provides an intuitive handle to both rationalize the interaction and streamline the experimentation.

Following this simple principle, the assembly of an ionic colloidal crystal requires only three ingredients: (1) oppositely charged particles, (2) a non-ionic surfactant that forms a uniform brush onto the surface of the particles and (3) salt to set the range  $\lambda_D$  of the electrostatic interactions. In a prototypical self-assembly experiment, a block copolymer (Pluronic F108) adsorbs onto a set of oppositely charged polystyrene (PS) microspheres ( $r \approx 500$  nm), forming a brush.

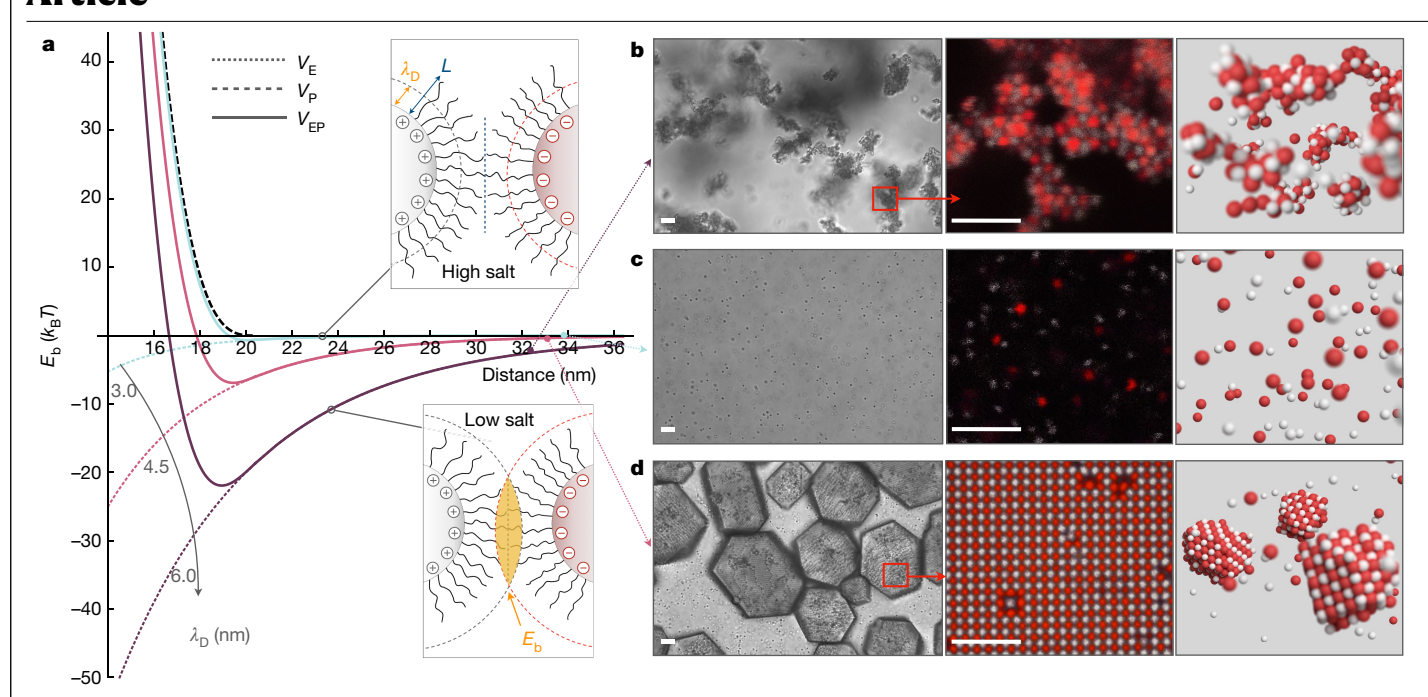


**Fig. 1**| **Polymer-attenuated Coulombic self-assembly. a**, Oppositely charged particles separated by a polymer spacer form a tunable ionic bond. Their pair potential  $(V_{\rm EP})$  comprises polymer repulsion  $(V_{\rm P})$  and Coulombic attraction  $(V_{\rm E})$ . Plots are calculated for a constant polymer brush length L=10 nm and increasing Debye screening lengths  $\lambda_{\rm D}$  of 3.0, 4.5 and 6.0 nm. For each

value of  $\lambda_{\rm D}$ , the corresponding  $V_{\rm EP}$  minima represent the ionic bond strength  $E_{\rm b}$ . **b–d**, From left to right: bright field microscopy, confocal microscopy and computer simulations of oppositely charged F108-grafted PS spheres at  $\lambda_{\rm D}$  = 6.0 (**b**), 3.0 (**c**) and 4.5 (**d**). Scale bars, 4  $\mu$ m.

The colloids are then equilibrated in sodium chloride (NaCl) solutions and simply mixed together. After mixing, the fate of the binary suspension is set by the salt concentration in the system. We observe three distinct assembly behaviours that are consistent with the relative bond energies calculated using our model. At low salt concentrations ( $\leq$ 4.3 mM),  $E_b$  is much larger than the thermal energy  $k_BT$ , causing the particles to bind irreversibly. What follows is a catastrophic flocculation that yields the macroscopic heteroaggregates shown in Fig. 1b. Increasing the salt concentration ( $\geq$ 4.9 mM) reduces  $E_b$ , leading to a less intuitive scenario whereby oppositely charged particles coexist in a stable suspension (Fig. 1c). In between these two regimes, we find

a narrow window of salinities in which oppositely charged particles behave as model ions, self-assembling into perfectly ordered ionic solids (Fig. 1d). The emergence of vibrant structural colours within a sample (Extended Data Fig. 1, Supplementary Video 1) easily reveals this 'Goldilocks zone', which—assuming a brush length L=10 nm for Pluronic F108—is characterized by bond energies of about  $8k_{\rm B}T$ . When left undisturbed, the oppositely charged particles condense within hours from mixing, forming millimetre-sized crystalline solids in a matter of days. Particles with stronger attraction initially produce gels that can anneal over time into crystalline phases (Extended Data Fig. 2). Although the resultant crystal domains are smaller than the ideal case,

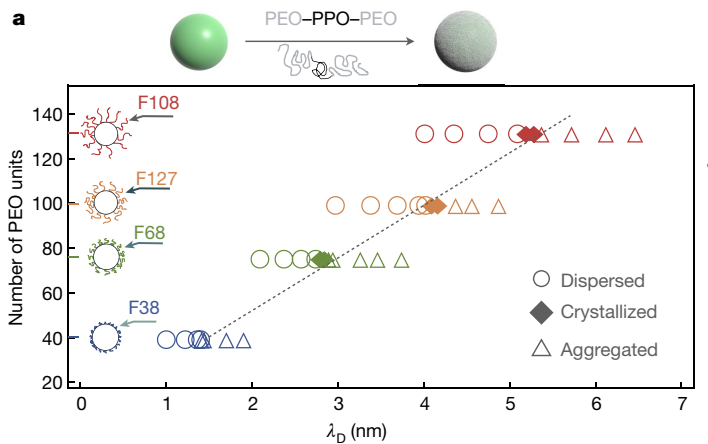
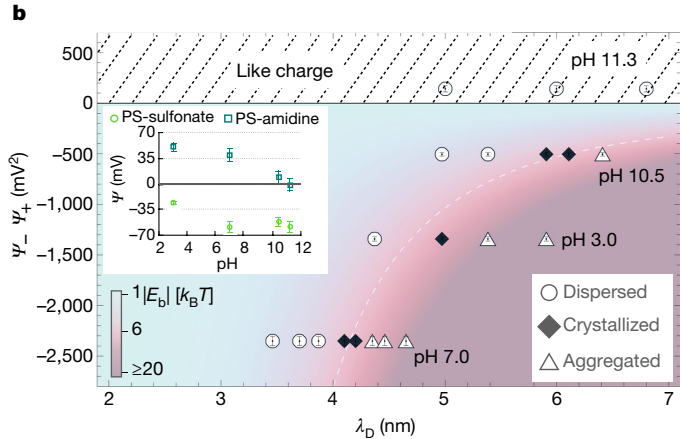


**Fig. 2** | **Tunable crystallization conditions. a**, Experimental phase diagram showing the assembly behaviour of oppositely charged PS as a function of  $\lambda_{\rm D}$  for different brush lengths. Polymer brushes are installed by grafting or physisorption of PEO-PPO-PEO triblock copolymers. The polymer architecture comprises an anchoring block (PPO) and a variable spacer block (PEO). Error bars ( $\pm 1$  s.d.) of the data points are smaller than the marker size. The dotted line is a linear fit between crystalline points. **b**, Assembly behaviour



of oppositely charged F108–PS colloids as a function of  $\lambda_D$  for different pH values. The colour gradient corresponds to the ionic bond energy  $E_b$  calculated assuming a brush length L=10 nm. The pH affects the surface potentials ( $\Psi_-$  and  $\Psi_+$ , inset) of the particles, which in turn set the amplitude of the electrostatic attraction. Error bars are  $\pm 1$  s.d. Crystallization occurs along a constant energy line (dotted) across a broad range of pH values. When the opposite charge is lost (here at pH 11.3) the suspension remains dispersed.

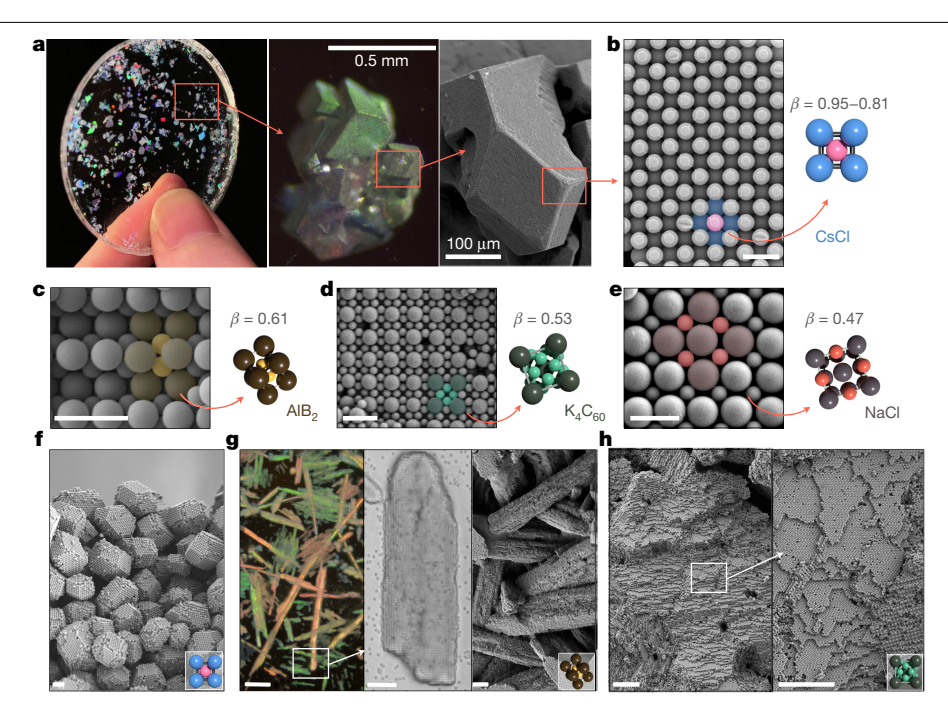


Fig. 3 | Fixed crystals. a, Fixed ionic colloidal crystals can be safely dried and manipulated. Left, a collection of millimetre-sized iridescent monocrystalline solids embedded in a matching refractive index epoxy resin (Supplementary Video 4). Middle and right, optical (middle) and SEM (right) micrographs showing the characteristic rhombic dodecahedral habit of a fixed CsCl crystal. b-e, Electron microscopy analysis reveals the exact structure of a series of ionic crystals formed at different  $\beta$  values, including CsCl ( $\mathbf{b}$ ), AlB<sub>2</sub>( $\mathbf{c}$ ), K<sub>4</sub>C<sub>60</sub>( $\mathbf{d}$ )

and NaCl (e). Scale bars,  $1 \mu m$ . f, SEM image showing rhombic dodecahedral CsCl crystallites. Scale bar, 3 µm. g, Left, optical micrograph of needle-like AlB<sub>2</sub> crystals imaged through crossed polarizers. Scale bar, 100 um, Middle, bright-field micrograph showing a growing AlB2 needle. Scale bar, 5 µm. Right, SEM image of fixed AlB<sub>2</sub> needles. Scale bar, 20 μm. **h**, SEM images of an exfoliated  $K_4C_{60}$  bulk crystal. Scale bars,  $10 \mu m$ .

this demonstrates that even when particles seem to aggregate chaotically, they remain sterically stabilized and continue to reconfigure, albeit slowly. In addition to direct visual clues, the nucleation and growth of ionic solids can be followed in much greater detail by in situ confocal microscopy, which allows differentiation between positive and negative species using two different fluorescent dyes (Fig. 1b-d, centre). Molecular dynamics simulations (Methods) further support our simple interaction model by revealing assembly behaviour that closely matches the experimental observations (Fig. 1b-d, right, Supplementary Video 2).

We perform crystallization experiments varying every ingredient in the system, including type of particle spacer, solvent conditions and building blocks. First, we explore the polymer-attenuated Coulombic self-assembly (PACS) energy landscape by systematically changing the length of the spacers. We select various polymer brush thicknesses through a series of Pluronic surfactants—namely F108, F127, F68 and F38, listed in decreasing length L. For each spacer, we rationally select the screening length to reach  $E_b$  of approximately  $8k_BT$  based on calculations from our model, and then fine-tune the experimental conditions until crystals nucleate. As expected, particles with shorter spacers require higher salt concentrations (that is, smaller values of  $\lambda_{\rm p}$ ) to reproduce the same self-assembly behaviour observed for longer spacers. We found a direct correlation between the spacer length and the values of  $\lambda_{\rm D}$  that cause crystallization, such that a constant ratio between the two produces equivalent interaction strengths (Fig. 2a). This confirms the simple argument that well-defined separation between oppositely charged particles allows for tunable electrostatic assembly. The linear relationship is clear across the three longest polymers, whereas the shortest polymer F38 fails to produce crystals, which we attribute to displacement flocculation because of its weak anchoring. We further test the robustness of PACS by assembling crystals under different pH conditions, as this strongly affects the native charge of the colloids.

Figure 2b shows that as we move away from neutral pH, one particle type rapidly loses charge-either the positive in basic conditions or the negative in acidic conditions. As the charge vanishes, the amplitude of the electrostatic attraction decreases, causing the crystals to disassemble. Increasing values of  $\lambda_D$  can compensate for the electrostatic decay, thus resulting in suspensions that crystallize at lower salt concentrations. By applying this criterion, crystals assemble over a broad range of pH conditions, with limits that are set only by the isoelectric points of the particles, beyond which the opposite charge is lost and electrostatic attraction vanishes. Finally, we mix and match particles of different compositions to demonstrate that PACS is not limited to PS microspheres, but applies to virtually any water-based colloidal system. Silica, 3-(trimethoxysilyl) propyl methacrylate (TPM) and PS particles with sizes ranging from 200 nm to 2 µm all successfully crystallize. In particular, the versatility of the method is best illustrated by the formation of hybrid crystals that incorporate both solid and liquid components (Supplementary Video 3).

The carefully balanced interactions that are required for colloidal self-assembly are often incompatible with any chemical or mechanical perturbation, requiring specific fixing mechanisms, ultimately limiting yield and scope<sup>21,22</sup>. By contrast, PACS interactions establish interparticle bonds with a convenient and general self-locking mechanism that bypasses this issue entirely. This distinctive feature is easily understood by considering the effect of removing salt on the pair potential of the particles. Because of the simple relationship between  $\lambda_{\rm D}$  and bond strength, crystals can be first assembled in salty water and then allowed to gradually harden by dilution or dialysis. In particular, we find that under deionized conditions, crystals become fixed solids, at which point they can be handled in solution and dried while retaining crystalline order. This process is irreversible, and crystals do not disassemble if salt is added back to the suspension, indicating permanent binding due to van der Waals interactions. Through this self-locking

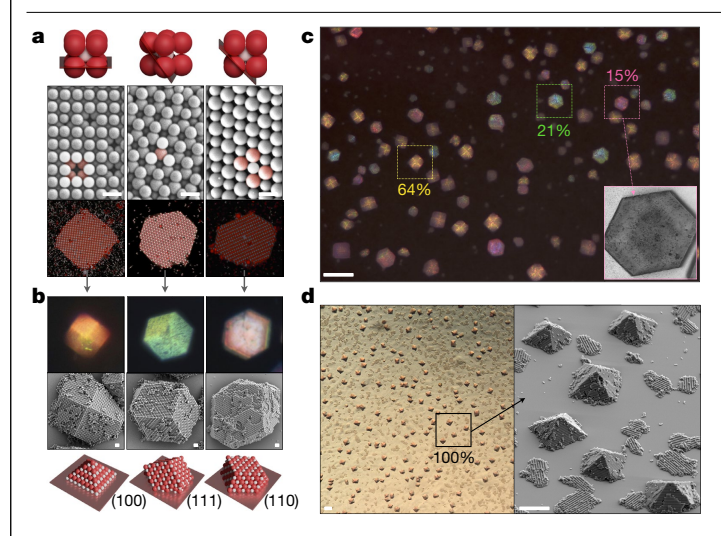


Fig. 4 | Heterogeneous nucleation of crystals. a, CsCl crystals growing on a  $negatively\,charged\,glass\,substrate.\,From\,left\,to\,right:\,(100),\,(111)\,and\,(110)$ planes are imaged by SEM (top) and confocal microscopy (bottom). False-coloured white and red particles highlight positive and negative species, respectively. Scale bars, 1 µm. On top of the SEM images, the schematics illustrate each plane relative to the unit cell of the crystal. **b**, Each crystal plane templates the growth of a macroscopic crystal with a characteristic shape. Crystals are captured by optical microscopy (top) and SEM (bottom). Scale bars, 1 µm. Renderings show the three-dimensional arrangement of the colloidal ions. c, Optical microscopy image showing crystals growing on a negatively charged glass substrate and the relative abundance of each crystal shape. Negative substrates favour the nucleation of crystal planes with a high planar density of positive particles. Scale bar, 40 µm. The inset shows the regular shape of a single crystal imaged by bright-field microscopy. d, An increased particle-substrate bond energy leads to the nucleation of only (100) planes. Left, bright-field micrograph of monodisperse pyramid-like crystals. Right, an SEM image of the fixed crystals, fully revealing their three-dimensional microstructure. Scale bars, 20 µm.

mechanism, we are able to observe that macroscopic colloidal ionic solids grow as single crystals and develop characteristic habits that resemble those of their atomic counterparts (Fig. 3, Extended Data Fig. 3). Dried products can be transferred to new media, such as matching refractive index liquids or flexible epoxy resins (Fig. 3a, Supplementary Video 4).

The structure of an atomic crystal varies according to the size of the constituent ions. Similarly, the structure of our ionic colloidal crystals is determined by the size ratio ( $\beta$ ) of the building blocks. For  $\beta$  between 0.95 and 0.81 colloidal crystals isostructural to caesium chloride (CsCl) nucleate, which rapidly develop with a rhombic dodecahedral habit (Fig. 3b, f), composed of faces from the (110) plane. At lower  $\beta$  values, the next structure observed occurs at  $\beta$  = 0.61, forming the aluminium diboride (AlB<sub>2</sub>) crystal structure, which develops with a characteristic needle-like habit<sup>23</sup> (Fig. 3c, g). At  $\beta$  = 0.53, an exotic K<sub>4</sub>C<sub>60</sub> phase is observed, which, when fractured, reveals large sheets of its (110) planes (Fig. 3d, h, Extended Data Fig. 4). Finally,  $\beta$  = 0.47 results in the nucleation of crystals with a familiar NaCl structure (Fig. 3e).

In addition to homogeneous nucleation from bulk suspensions, crystals can readily assemble via heterogeneous nucleation against charged substrates. This second self-assembly route allows us to bias the crystal growth along specific crystallographic directions, effectively shaping the growing solids. This is illustrated in Fig. 4a (see also Extended Data

Fig. 5), in which CsCl planes are selected by a negatively charged glass substrate-namely the (100), (111) and (110) planes-in descending order of planar density of positive particles. Each plane templates the growth of CsCl crystals with a specific orientation, resulting in their speciation into three distinct crystal types with characteristic colours and shapes; yellow squares (100), green hexagons (111) and pink hexagons (110) (Fig. 4b). Specific colouration in the species arises from the uniformly oriented crystals scattering light at the same angle. Counting the species based on colour and shape allows rapid determination of the relative yields, where substantially more (100) planes are nucleated due to their higher density of positive particles, followed logically by the (111) and (110) planes. Substrate influence is more pronounced when the interaction strength is increased, leading to the formation of purely (100) planes. We conclude that differing crystalline pyramids can be selected to self-assemble by surface attraction in experiments and simulations (Fig. 4c, Extended Data Fig. 5).

#### **Online content**

Any methods, additional references, Nature Research reporting summaries, source data, extended data, supplementary information, acknowledgements, peer review information; details of author contributions and competing interests; and statements of data and code availability are available at https://doi.org/10.1038/s41586-020-2205-0.

- Pauling, L. The principles determining the structure of complex ionic crystals. J. Am. Chem. Soc. 51, 1010–1026 (1929).
- Shevchenko, E. V. et al. Structural diversity in binary nanoparticle superlattices. Nature 439, 55–59 (2006).
- Kalsin, A. M. et al. Electrostatic self-assembly of binary nanoparticle crystals with a diamond-like lattice. Science 312, 420–424 (2006).
- Grzybowski, B. A. et al. Electrostatic self-assembly of macroscopic crystals using contact electrification. Nat. Mater. 2, 241–245 (2003).
- Go, D. et al. Programmable co-assembly of oppositely charged microgels. Soft Matter 10, 8060–8065 (2014).
- Månsson, L. K. et al. Preparation of colloidal molecules with temperature-tunable interactions from oppositely charged microgel spheres. Soft Matter 15, 8512–8524 (2019).
- Mihut, A. M. et al. Assembling oppositely charged lock and key responsive colloids: a mesoscale analog of adaptive chemistry. Sci. Adv. 3, e1700321 (2017).
- 8. Wang, Y. et al. Crystallization of DNA-coated colloids. Nat. Commun. 6, 7253 (2015).
- Leunissen, M. E. et al. Ionic colloidal crystals of oppositely charged particles. Nature 437, 235–240 (2005).
- Bartlett, P. & Campbell, A. I. Three-dimensional binary superlattices of oppositely charged colloids. Phys. Rev. Lett. 95, 128302 (2005).
- Bartlett, P., Ottewill, R. H. & Pusey, P. N. Superlattice formation in binary-mixtures of hard-sphere colloids. Phys. Rev. Lett. 68, 3801–3804 (1992).
- Pusey, P. N. & Vanmegen, W. Phase-behavior of concentrated suspensions of nearly hard colloidal spheres. Nature 320, 340–342 (1986).
- 13. Sacanna, S. et al. Lock and key colloids. Nature 464, 575-578 (2010).
- de Nijs, B. et al. Entropy-driven formation of large icosahedral colloidal clusters by spherical confinement. Nat. Mater. 14, 56–60 (2015).
- Harper, E. S., van Anders, G. & Glotzer, S. C. The entropic bond in colloidal crystals. Proc. Natl Acad. Sci. USA 116, 16703–16710 (2019).
- Nykypanchuk, D. et al. DNA-guided crystallization of colloidal nanoparticles. Nature 451, 540–552 (2008)
- Wang, Y. F. et al. Patchy particle self-assembly via metal coordination. J. Am. Chem. Soc. 135, 14064–14067 (2013).
- Rogers, W. B., Shih, W. M. & Manoharan, V. N. Using DNA to program the self-assembly of colloidal nanoparticles and microparticles. Nat. Rev. Mater. 1, 16008 (2016).
- 19. Hunter, R. J. Foundations of Colloid Science 2nd edn (Oxford Univ. Press, 2001)
- Milner, S. T., Witten, T. A. & Cates, M. E. Theory of the grafted polymer brush. Macromolecules 21, 2610–2619 (1988).
- Vutukuri, H. R. et al. Bonding assembled colloids without loss of colloidal stability. Adv. Mater. 24, 412-416 (2012).
- McGinley, J. T. et al. Crystal-templated colloidal clusters exhibit directional DNA interactions. ACS Nano 9, 10817–10825 (2015).
- Seo, S. E. et al. Non-equilibrium anisotropic colloidal single crystal growth with DNA. Nat. Commun. 9, 4558 (2018).

**Publisher's note** Springer Nature remains neutral with regard to jurisdictional claims in published maps and institutional affiliations.

© The Author(s), under exclusive licence to Springer Nature Limited 2020

### **Methods**

#### **PACS** model

We estimate the repulsive potential  $V_P$  in Fig. 1a using the Alexander-de Gennes polymer brush model<sup>24–26</sup>:

$$\frac{V_{\rm P}}{k_{\rm B}T} = \frac{16\pi r L^2 \sigma_2^3}{35} \left[ 28 \left( \left( \frac{2L}{h} \right)^{\frac{1}{4}} - 1 \right) + \frac{20}{11} \left( 1 - \left( \frac{h}{2L} \right)^{\frac{11}{4}} \right) + 12 \left( \frac{h}{2L} - 1 \right) \right], \quad (1)$$

 $0 \le h \le 2L$ 

where the PS radius r is measured by electron microscopy ( $r_{\text{SEM}}$ = 250 nm), the thickness of the F108 brush L is taken equal to 10 nm (ref.  $^{27}$ ) and the polymer surface density  $\sigma$  is estimated as 0.09 poly(ethylene oxide) (PEO) chains per nm² (ref.  $^{28}$ ). The attractive electrostatic potential  $V_{\text{E}}$  is obtained by approximating the surface potentials of the particles ( $\Psi_{+}$  and  $\Psi_{-}$ ) with the measured zeta potentials (+39 mV and –59 mV, respectively).

#### Colloidal model systems

The principal model systems consist of PS particles synthesized via surfactant-free emulsion polymerization. For example, 600-nm-diameter positive spheres were made from a single-step reaction comprising 500 ml of deionized water, 50 ml of styrene monomer (≥99% from MilliporeSigma) and 0.5g of the radical initiator 2,2'-azobis(2-methylpropionamidine) dihydrochloride (97% from MilliporeSigma). All the ingredients were mixed in a three-neck round-bottom flask, heated to 60 °C and stirred at 330 rpm under nitrogen overnight. After the reaction had concluded, the particles were washed via repeated sedimentation and resuspension cycles. Control over the PS size was achieved by varying the monomer concentration, reaction temperature or reaction time. Negatively charged PS particles were produced in the same fashion, replacing 2,2'-azobis(2-m ethylpropionamidine) dihydrochloride with an equivalent weight amount of potassium persulfate (≥99% from MilliporeSigma). Fluorescent labelling of the PS systems was achieved by a swell-deswell method. In brief, fluorescent dyes dissolved in tetrahydrofuran (THF) were added to particles stabilized with Pluronic F108 (MilliporeSigma) to a final concentration of 30% v/v THF, then diluted by a factor of five before washing the particles via multiple sedimentation and resuspension cycles to set them in pure water. The fluorescent dyes used were rhodamine-labelled aminostyrene and 7-nitrobenzo-2-oxa-1.3-diazole-2-(methylamino)ethanol. Rhodamine-labelled aminostyrene was prepared by adding 48 mg of rhodamine B isothiocyanate (mixed isomers from MilliporeSigma), 12 mg of aminostyrene (97% from Mil $lipore Sigma) \, and \, 0.1 \, ml \, of \, tetramethylammonium \, hydroxide \, (25 \, wt\% \,$ in water from MilliporeSigma) to 200-proof ethanol (10 ml), and stirring the mixture overnight, which was then stored at 5 °C. Monodispersed oil droplets used in the assembly of liquid-solid composite crystals (Supplementary Video 3) were prepared through the condensation of 3-(trimethoxysilyl) propyl methacrylate (TPM, ≥98% from Millipore-Sigma), by adding 80 µl of ammonia (28 wt%) to 320 ml of deionized water, followed by the addition of 600 µl of TPM. This mixture was magnetically stirred for 1 h, which resulted in the nucleation and growth of droplets of approximately 1 µm in diameter. Fluorescent labelling was achieved with rhodamine B isothiocyanate, coupled to 3-aminopropyl trimethoxysilane for covalent binding to the TPM network. The droplets can be used directly or solidified via a radical polymerization. To use the liquid droplets directly, the emulsion was gently centrifuged, the supernatant removed and the droplets resuspended in deionized water. This wash cycle was repeated three times. To solidify the TPM particles, 20 mg of azobisisobutyronitrile (98% from Millipore Sigma) was added to the suspensions and gently stirred for 5 min; then the suspension was left in a sealed container at 80 °C for 4 h. The particles were then washed in the manner described above.

#### Self-assembly of ionic colloidal crystals

Positive and negative PS spheres were separately equilibrated in a solution containing 0.03 mM of Pluronic F108 and the desired amount of NaCl, typically 3–5 mM. After 1h, the suspensions were rapidly mixed together while vortexing and then allowed to crystallize undisturbed in various containers (for example, glass vials, NMR tubes, Eppendorf centrifuge tubes or Petri dishes). Occasionally, samples were sealed in glass capillaries (VitroCom) and monitored over time via optical microscopy. Capillaries were pretreated with a hydrophobizing agent to facilitate the formation of a polymer brush when exposed to Pluronic solutions. The typical hydrophobization protocol consisted of a 20-min exposure to trichloromethyl silane vapour inside of a moisture-free sealed chamber.

Assembly experiments involving particles with different brush lengths were performed using PS with grafted polymers. While not necessary for the successful assembly of crystals, grafting ensures that particles maintain a fully saturated surface regardless of polymer solubility. This allows for a fair comparison between particles that carry different polymer spacers. Pluronic surfactants were permanently grafted to the surface of PS particles via a swell-deswell method<sup>29</sup>. The specific surfactants, namely, F108, F127 and F68, were added to the PS suspensions at their critical micelle concentration (3.4 mM, 0.8 mM and 20 mM, respectively), then THF was added to the suspension to a final concentration of 50% v/v. The suspensions were left to equilibrate for 1 h, and the THF was diluted to below 5% v/v before washing the particles via centrifugation and resuspension. A polymer solution at the critical micelle concentration was used for the first wash until the THF was reduced to below 1% v/v, then particles were finally set in pure water after three more wash cycles. Pluronic F38 was not grafted to the particles because it failed to produce crystals even when present in high concentrations (~3 mM). We believe that F38 is too small to serve as an effective spacer for our PS model system, so it was not further investigated. The assembly of polymer-grafted PS followed a similar protocol as for the assembly of PS with physisorbed polymers. Typically, two PS suspensions (for example, 3 wt% 550-nm-diameter negative PS and 1.6 wt% 450-nm-diameter positive PS) with the same grafted polymer were equilibrated for 30 min in an excess of that polymer at a concentration of 80 µM and at a variety of salt concentrations based on the desired  $\lambda_{\rm D}$ . After equilibration, the oppositely charged suspensions were rapidly mixed and immediately sealed in hydrophobized capillaries using hot wax. The capillaries were left undisturbed for 12 h. at which time the assembly behaviour was observed via optical microscopy.

Our assembly strategy was successful with different types of polymers as long as they provided adequate spacing. The triblock copolymers described above have an A–B–A architecture, PEO–PPO–PEO, in which the central PPO block serves as the polymer anchor. We assembled ionic colloidal crystals, however, also using the polymer Brij s100, which has an A–B structure comprising a 100-unit PEO tail and a stearyl head group. Notably, crystallization occurs at an equivalent salt concentration to Pluronic F127, which has equivalent length PEO chains, suggesting Brij forms a polymer shell of similar thickness.

#### **Fixing crystals**

Bulk samples have their supernatant slowly diluted with deionized water, avoiding large-scale flows and shear that would affect the sedimented crystal. The supernatant can be carefully exchanged, removing all the salt, at which point crystals are robust enough to be resuspended and dried. Crystals inside of sealed capillaries are fixed by submerging the capillary in deionized water, and breaking the capillary's ends, taking care to not disturb the product as much as possible. The sample is allowed to equilibrate overnight, then removed to dry slowly for another day. The capillary can then be opened by scoring the sides with a glass cutter and cleaving off the top, exposing the fixed crystalline product. Epoxy resin (Norland 73) can be poured directly onto fixed

dried crystals. Bubbles can form as the resin permeates through the crystal, so the infusion was allowed to proceed for typically 15 min to allow air bubbles to evacuate. The resin was then polymerized through 5 min of ultraviolet light exposure.

#### **Imaging and characterization**

Optical images and videos were acquired using a Leica DMI3000 inverted microscope equipped with differential interference contrast optics and a high-resolution camera (Hamamatsu ORCA Flash4.0 sCMOS). Assembled crystals were typically imaged through crossed polarizers using a Nikon D5300 camera optically coupled to the microscope. Fixed crystals were imaged by electron microscopy using a MER-LIN (Carl Zeiss) field emission SEM. Fluorescent images were taken using a Leica SP8 confocal microscope. Zeta potentials were measured using a Malvern Zetasizer Nano ZS.

#### **Computer simulations**

Simulations were performed using HOOMD-blue v2.5 (compiled in single precision)30, using a single graphics processing unit. The pair interaction between two particles of types N (negative) and P (positive) with radius  $r_N$  and  $r_P$  was defined by adding  $V_F$  to the potentials given by equation (1), using HOOMD-blue's tabulated potential option (with 1,000 interpolation points between the close touching distance,  $r_N + r_P$ , and  $rN + r_p + 20\lambda_D$ ). For the steric repulsion term, we use a brush length L = 10 nm, and a brush density  $\sigma = 0.09$  nm<sup>-2</sup>. For the electrostatics, we used surface potentials  $\Psi_{-} = -50 \,\text{mV}$  and  $\Psi_{+} = +50 \,\text{mV}$ , a dielectric constant of 80 and a mixing rule for the pre-factor  $r = 2/(1/r_N + 1/r_P)$ . Unless otherwise stated, simulations were initiated as having 8,000 spherical particles on a simple cubic lattice such that the packing fraction is  $\phi$ . with random assignments of particle type. Values of  $\phi$  of either 0.001 or 0.003 tended to give a good amount of nucleation while still leaving enough free particles to assemble some crystals. Heterogeneous nucleation on a charged surface was modelled by adding an attractive Lennard-Jones wall for N (P) particles in the centre of the simulation box pointing up and down, with Lennard-Jones parameters  $\sigma = 2r_{N(P)}$ , and a tunable  $\varepsilon$ . For Extended Data Fig. 2e, we also added a repulsive potential to the other particle of type P (N) with the same parameters but where the potential was shifted up and cut off at its minimum distance  $r = 2^{1/6} \sigma_{P(N)}$ .

## **Data availability**

The data that support the findings of this study are available from the corresponding author on request.

- Alexander, S. Polymer adsorption on small spheres—scaling approach. J. Phys. (Paris) 38, 977–981 (1977).
- Gennes, P. G. D. Stabilité de films polymère/solvant. C. R. Acad. Sci. II 300, 839–843 (1985)
- Kleshchanok, D., Tuinier, R. & Lang, P. R. Direct measurements of polymer-induced forces. J. Phys. Condens. Matter 20, 073101 (2008).
- Barnes, T. J. & Prestidge, C. A. PEO-PPO-PEO block copolymers at the emulsion dropletwater interface. *Langmuir* 16, 4116–4121 (2000).
- Stenkamp, V. S. & Berg, J. C. The role of long tails in steric stabilization and hydrodynamic layer thickness. *Langmuir* 13, 3827–3832 (1997).
- Kim, A. J., Manoharan, V. N. & Crocker, J. C. Swelling-based method for preparing stable, functionalized polymer colloids. J. Am. Chem. Soc. 127, 1592–1593 (2005).
- Glaser, J. et al. Strong scaling of general-purpose molecular dynamics simulations on GPUs. Comput. Phys. Commun. 192, 97-107 (2015).

Acknowledgements This work was supported primarily by the NSF CAREER award DMR-1653465. We are grateful for shared facilities provided through the Materials Research Science and Engineering Center (MRSEC) and MRI programmes of the National Science Foundation under award numbers DMR-1420073 and DMR-0923251. Computational resources were provided by New York University High Performance Computing. J.P. thanks the Sloan Foundation for support through grant FG-2017-9392 and the National Science Foundation under grant number DMR-1554724. We thank H. Kanwal for assistance in self-assembly experiments and H. Chun for comments on the manuscript and discussions.

**Author contributions** S.S. led the research. T.H. and S.S. conceived the PACS idea. T.H. synthesized the colloidal systems, and designed and performed the crystallization experiments. G.M.H. designed, performed and analysed the simulations, with input from T.H. and S.S. J.P. developed the theoretical model. The manuscript was written by S.S. and T.H. All authors discussed the results and commented on the manuscript.

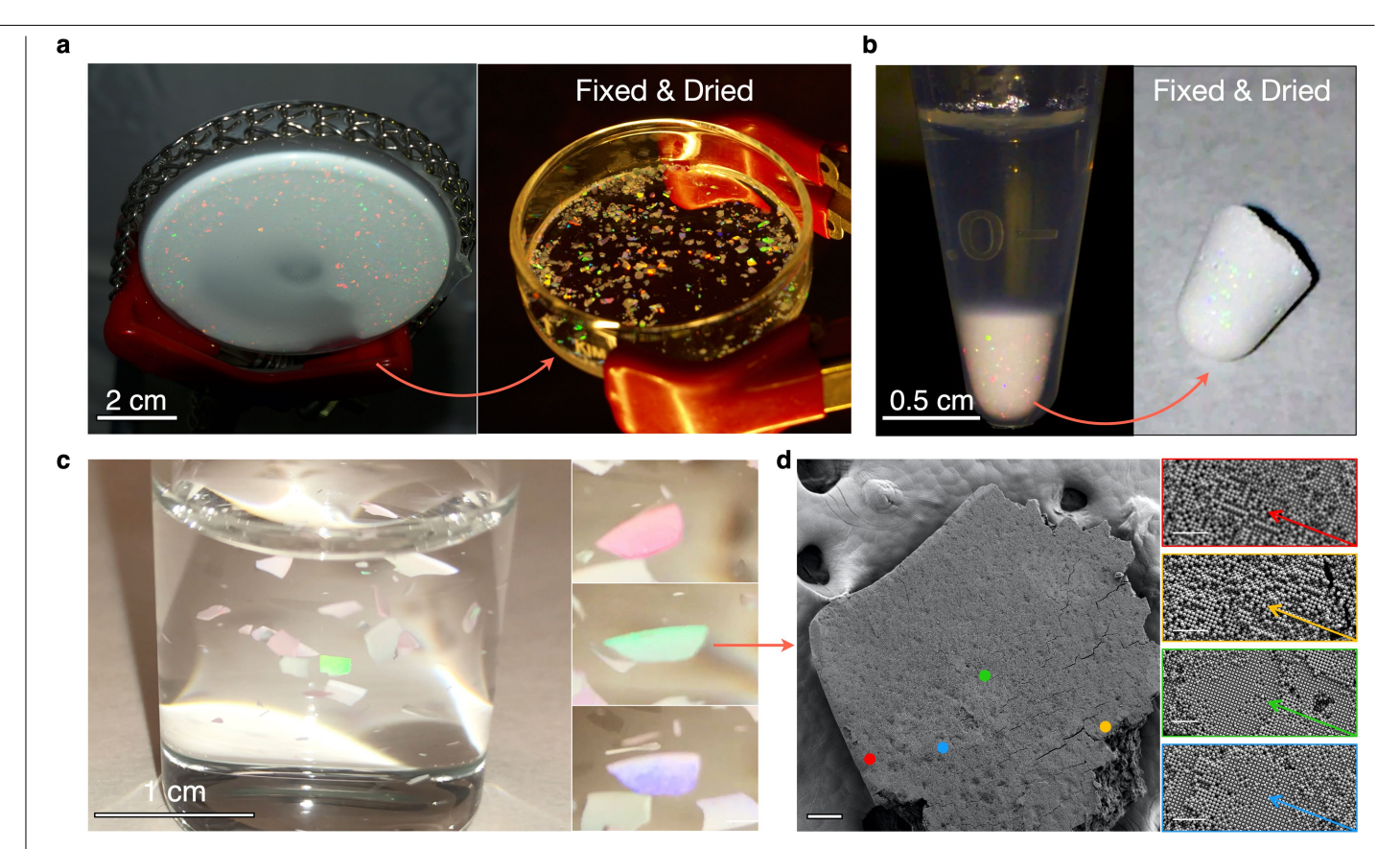
Competing interests The authors declare no competing interests.

#### Additional information

**Supplementary information** is available for this paper at https://doi.org/10.1038/s41586-020-2205-0.

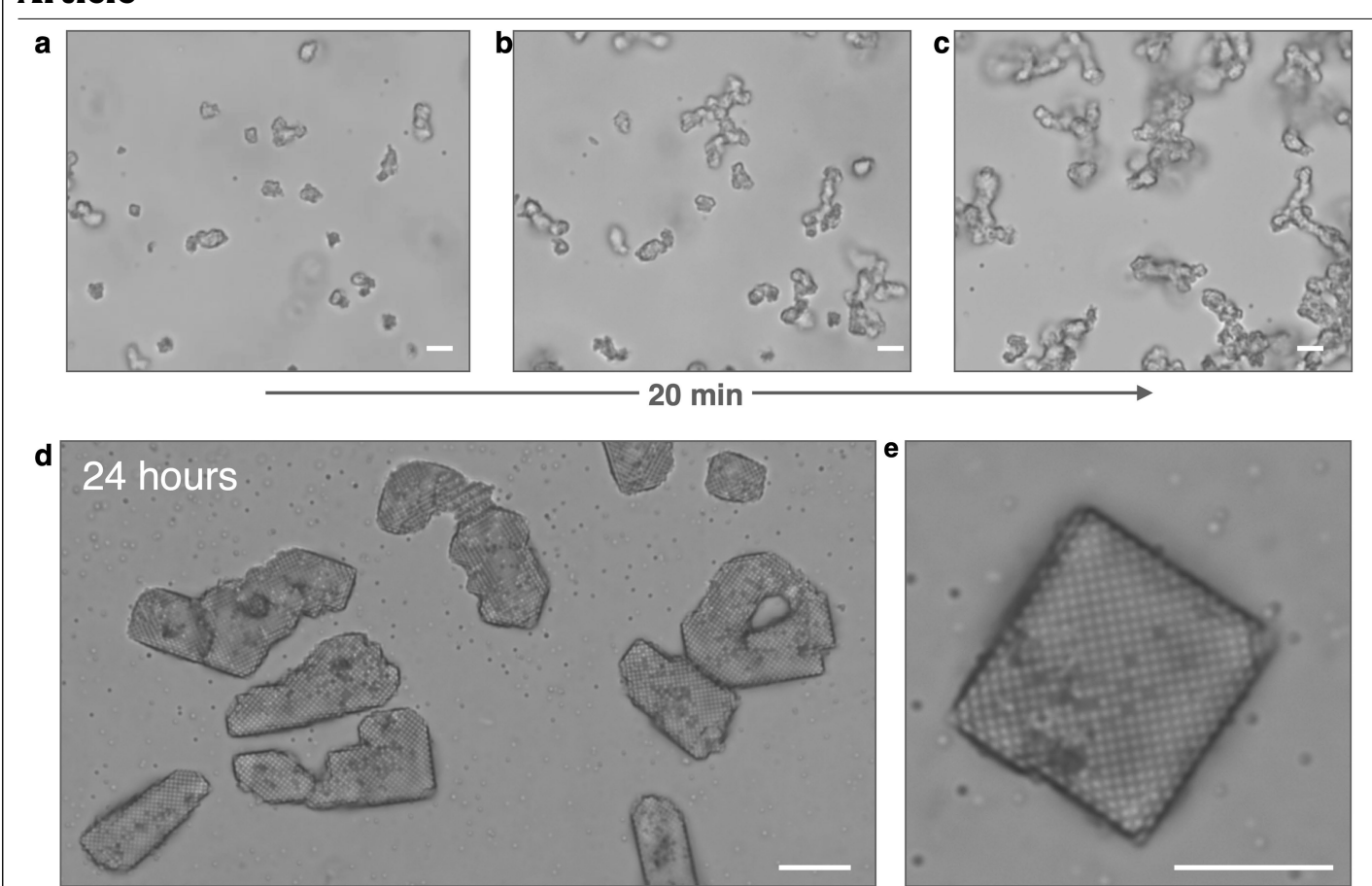
Correspondence and requests for materials should be addressed to S.S.

Reprints and permissions information is available at http://www.nature.com/reprints.



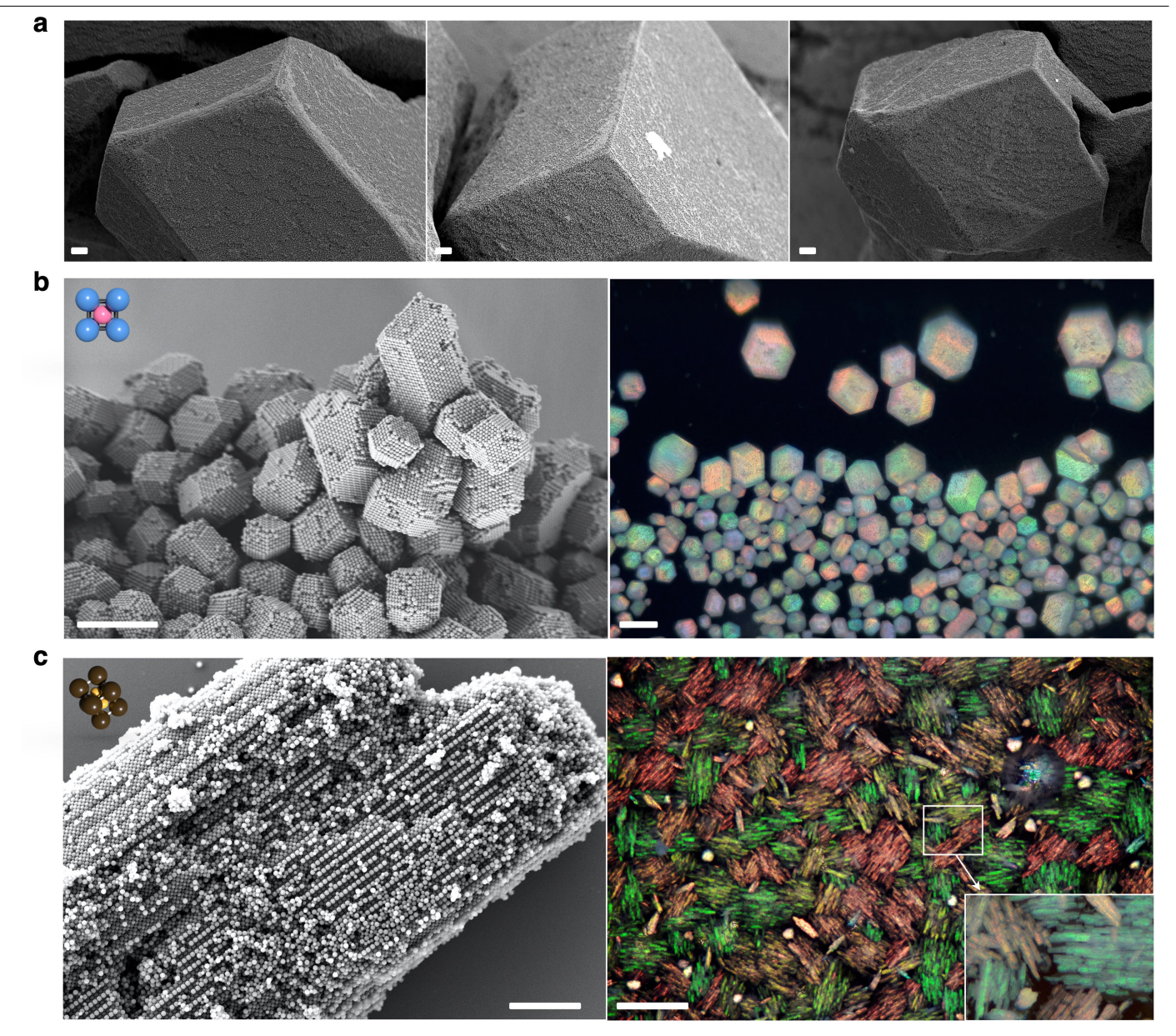
 $\label{lem:extended Data Fig. 1} I ridescent macroscopic single crystals. a, Single crystals with millimetre diameters visible on the bottom of a 10-cm Petri dish. Boundaries between single crystals are clear through the uniformly coloured regions of the Voronoi pattern that forms. b, The crystallinity of the bulk sediment is visible through iridescence when left undisturbed. At 5 mM of NaCl, the assembly is still reconfiguring and delicate. After fixing through dilution and slowly drying, the hardened sediment retains iridescence, denoting retention of crystalline order. In air versus water, iridescence is muted due to a$ 

large refractive index mismatch.  ${f c}$ , Fixed crystals dispersed and freely floating in density matched water (Supplementary Video 4). Slow rotation of the crystals reveals their colouration's angle dependence, displaying vibrant and uniformly coloured red, green, and blue iridescence as they rotate.  ${f d}$ , SEM micrograph of a single crystal, examined at high magnification at four locations across the surface of the crystal. At each site, the crystal displays the same crystallographic plane and angle, demonstrating that the whole crystal is in register. Scale bar,  $100~\mu m$ . Scale bar of high magnification sites,  $5~\mu m$ .



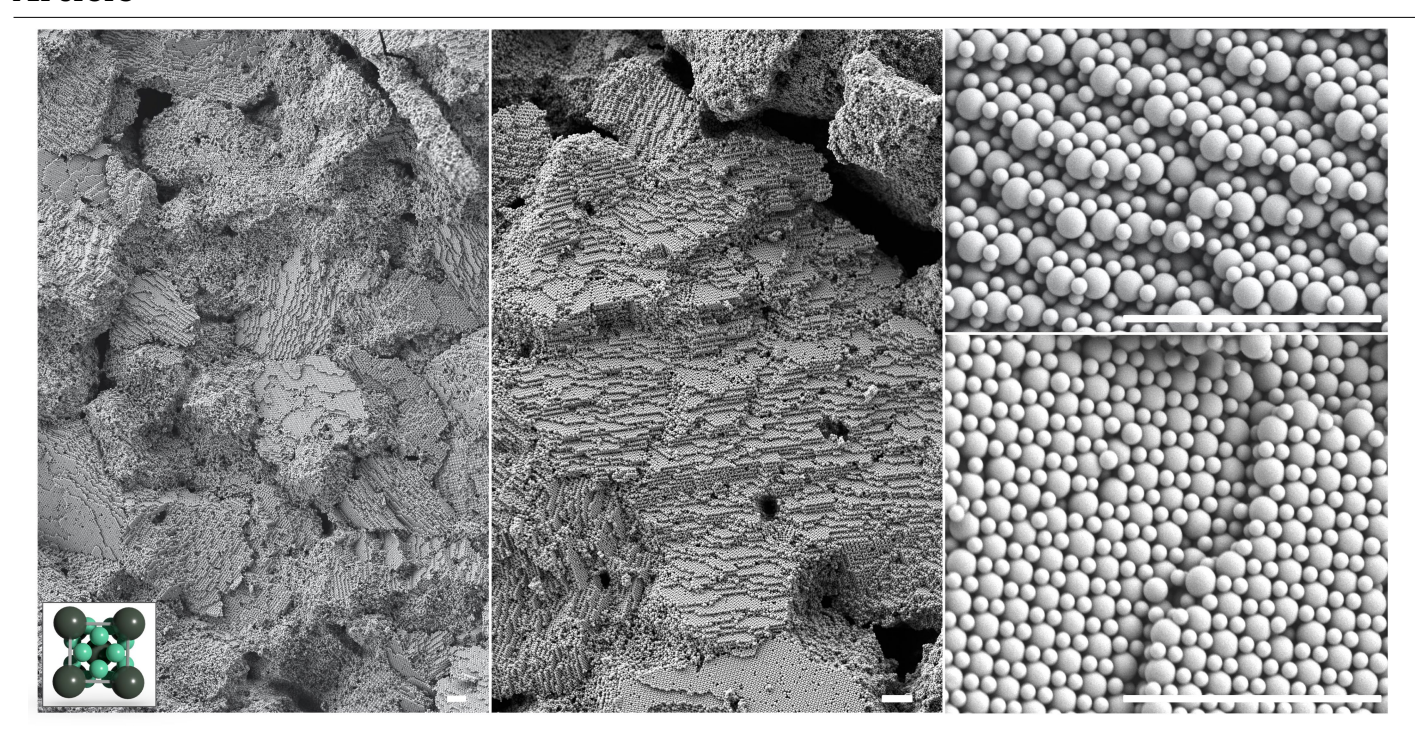
 $\label{lem:extended Data Fig. 2 | Crystals annealing with strong electrostatic attraction. a-c, A 20-min time lapse of particles calculated to have a potential well depth of 12 kT. Coagulation occurs immediately after mixing and disordered heteroaggregates rapidly sediment. Although no order is present, a small degree of reconfiguration can be observed on the single-particle level.$ 

Images were taken at 1 min (a), 5 min (b) and 20 min (c). d, After 24 h, the sample has crystallized. e, Crystals produced in this manner display the (100) plane due to the strong electrostatic attraction to the negatively charged substrate. Scale bars, 10  $\mu m$ .

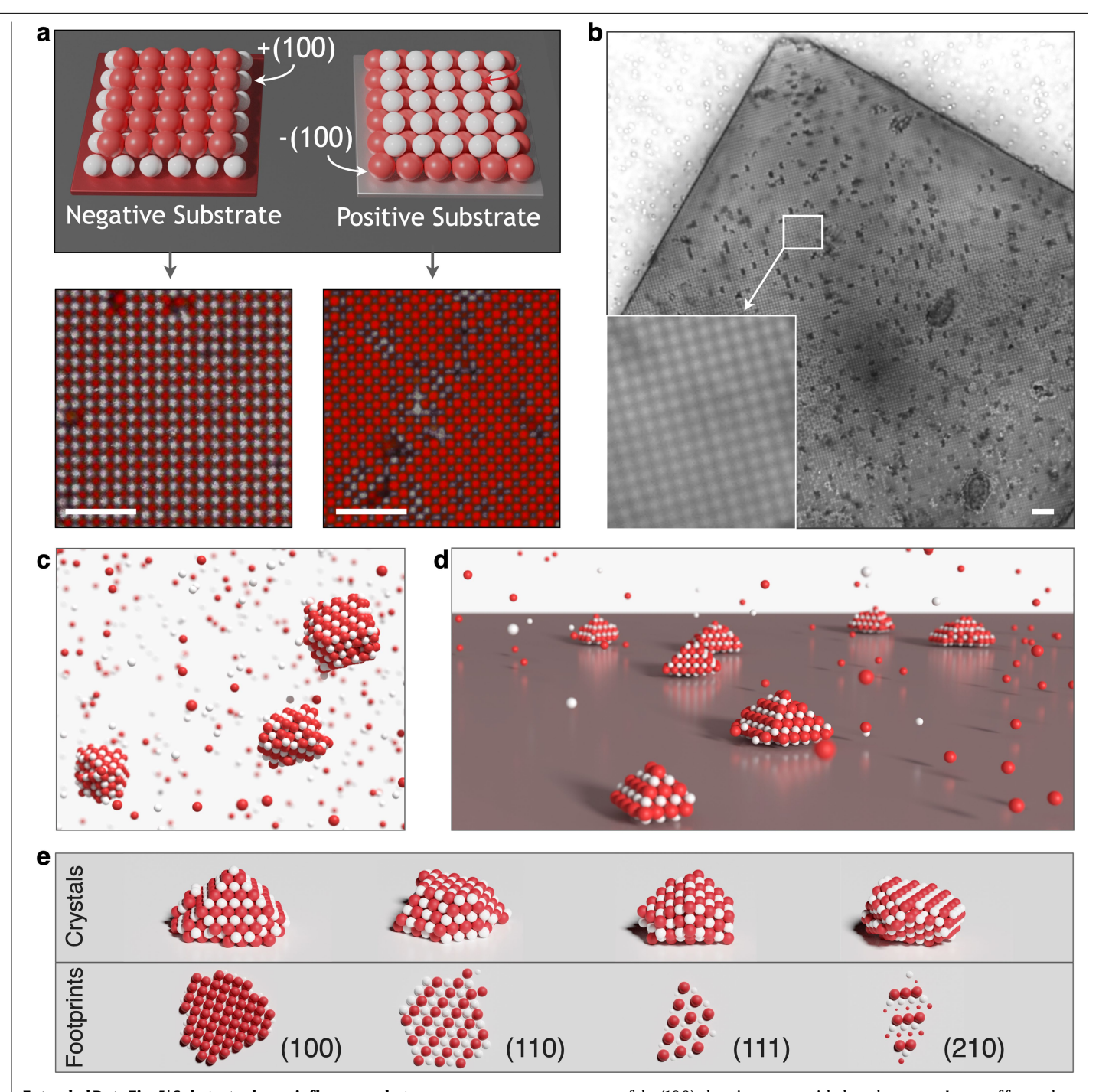


**Extended Data Fig. 3** | **Crystal habits. a**, SEM micrographs of crystal facets from a rhombic dodecahedral CsCl ionic colloidal crystal. Scale bars, 10  $\mu$ m. **b**, Left, SEM micrograph of small CsCl crystals with dodecahedral habit. Close inspection reveals sides comprised of the (110) plane. Scale bar, 10  $\mu$ m. Right, optical micrograph of CsCl crystals. Scale bar, 100  $\mu$ m. **c**, Left, SEM micrograph

of an AlB $_2$  needle. Close inspection reveals crystals growing with a railroad pattern characteristic of their (1010) plane. Scale bar, 3  $\mu$ m. Right, optical micrograph of needles growing aligned in bunches and reveal the same colour, in sets of red and greens depending on the angle of orientation. Scale bar, 120  $\mu$ m.



 $\textbf{Extended Data Fig. 4} \\ \textbf{Layered pattern of K}_4\textbf{C}_{60} \textbf{ crystals. SEM micrographs of a bulk K}_4\textbf{C}_{60} \textbf{ ionic colloidal crystal captured at increasing magnification. Cleavage of the crystals reveals sheets of the (110) plane. Scale bars, 5 \, \mu\text{m}.$ 



**Extended Data Fig. 5** | **Substrate charge influence on heterogeneous nucleation of crystals. a**, Schematic of substrate charge influence, where the (100) plane of either charge grows on an oppositely charged substrate. Bottom left, (100) plane of positive (white) particles growing on a naturally negatively charged glass substrate. Bottom right, glass surface treated with aminosilane for positive charge nucleates a negative (100) plane. Scale bars, 6  $\mu$ m. **b**, Bright field microscopy image showing a macroscopic crystal nucleated on a negatively charged substrate. The magnified inset reveals the characteristic

pattern of the (100) plane in contact with the substrate. **c**, Image of faceted CsCl crystals that nucleate spontaneously in simulation, where  $\lambda_{\rm D}$  = 4.5 nm,  $r_{\rm N}$  = 500 nm and  $r_{\rm P}$  = 430 nm. **d**, Heterogeneous nucleation is observed when a model attractive surface is added under the same conditions as **b**. The attractive surface has a strength of  $\varepsilon$  = 5 $k_{\rm B}T$  for positive particles. **e**, Structures heterogeneously assembled relative to these facets were observed with an attractive and repulsive strength of  $\varepsilon$  = 3 $k_{\rm B}T$  and with an increased size of N particles such that the ratio of  $\sigma_{\rm N}/\sigma_{\rm P}$  = 1.24.